RSC Advances

PAPER

View Article Online
View Journal | View Issue

Cite this: *RSC Adv.*, 2026, **16**, 11779

Interfacial ion diffusion and rapid charge transfer kinetics of the hydrothermally synthesized heterostructured Bi_2WO_6/Bi_2O_3/MXene composite for next-generation pseudocapacitors

Komal Ali Rao, *[a] Muhammad Ehsan Mazhar, *[a] Javed Ahmad,[a] Muhammad Imran Khan, [b] Muhammad Bilal,[c] Adel A. El-Zahhar,[d] Majed M. Alghamdi,[d] Waseem Abbas,[a] Iqra Nawaz[a] and Haleema Riaz[e]

MXenes are potential electrode materials for supercapacitors because of their significant conductivity, large surface area, layered structure and chemical stability. Nonetheless, their strong interlayer interactions result in the restacking of MXene sheets, thereby hindering electrolyte diffusion as well as charge accumulation. Metal oxide nanostructures can improve interlayer spacing as well as electrolyte diffusion. In this work, a heterostructured Bi_2WO_6/Bi_2O_3/MXene composite electrode was successfully prepared through a hydrothermal method to hinder the restacking of MXene, facilitate ionic diffusion, and increase specific capacitance. The formation of the composite, the coexistence of the crystal phases in Bi_2WO_6, and the robust interactions between Bi_2WO_6 and MXene ($Ti_3C_2T_x$) were verified through structural and compositional characterization techniques, such as X-ray diffraction (XRD) and X-ray photoelectron spectroscopy (XPS). Morphological characterization demonstrated the effective anchoring of Bi_2WO_6/Bi_2O_3 nanostructures on MXene surfaces, leading to increased ion-channel pathways without the agglomeration of MXene layers. The Bi_2WO_6/Bi_2O_3/MXene electrode showed markedly enhanced charge storage performance, including higher specific capacitance, improved rate capability, and reduced internal resistance compared to pristine Bi_2WO_6/Bi_2O_3. This improvement originated from the synergistic interaction between redox-active Bi_2WO_6/Bi_2O_3 and the conductive MXene network, enabling efficient ion–electron transport and excellent cycling stability, thereby making the electrode a promising electrode for high-performance supercapacitors.

Received 12th January 2026
Accepted 16th February 2026

DOI: 10.1039/d6ra00310a

rsc.li/rsc-advances

1 Introduction

The growing demand for energy due to increasing population and industrialization has created unprecedented pressure on conventional fossil fuels. The increased demand for fossil fuels has not only triggered the exhaustion of resources but also increased the severity of environmental issues like greenhouse gas emissions. Thus, the development of sustainable, eco-friendly, and renewable energy resources has become a top priority.[1–4] To this end, electrochemical energy storage (EES) technology, in the form of batteries, fuel cells (*e.g.*, SOFCs and biofuel cells) and supercapacitors (SCs), has been identified as an efficient means for the conversion as well as the storage of energy.[5,6] The continuous improvement in electrochemical material and device designs has made it possible for such modern EES systems to achieve higher power density, longer life, and better safety than traditional systems.[7,8]

Among the various EES technologies, supercapacitors have received much attention owing to their distinct ability to overcome the difference in the performance characteristics between capacitors and batteries. Supercapacitors possess higher energy density than dielectric capacitors and much higher power density and durability than batteries; hence, they are perfect for applications in portable electronics and electric vehicles. On the basis of charge storage mechanisms, SCs are generally divided into electrical double-layer capacitors (EDLCs), pseudo-capacitors, and battery-type capacitors. While EDLCs store charge *via* an electrostatic adsorption process interfacing the electrode and electrolytes, pseudocapacitors use fast and reversible faradaic reactions. Battery-type capacitors operate *via*

[a]*Institute of Physics, Bahauddin Zakariya University, Multan 60800, Pakistan. E-mail: komalrao49@gmail.com; dr.ehsan@bzu.edu.pk*

[b]*Research Institute of Sciences and Engineering (RISE), University of Sharjah, Sharjah 27272, United Arab Emirates*

[c]*School of Engineering and Materials Science, Queen Marry University of London, E1 4NS, UK*

[d]*Department of Chemistry, College of Science, King Khali University, Abha 61413, Saudi Arabia*

[e]*Department of Chemistry, The Government Sadiq College Women University Bahawalpur, 63100, Pakistan*

relatively slow ion intercalation reactions.[9–12] Considering this background, mixed systems combining both EDLC and pseudocapacitive characteristics have proven to be highly useful to increase the overall capacitance of the material, along with its charge–discharge rates.[13,14]

To further improve SCs' performance, ongoing research efforts are centered on two aspects: (i) advanced electrode material design and (ii) optimisation of ion transport kinetics at the electrode/electrolyte interface. Various electroactive substances such as conducting polymers, carbon-based substances, and metal oxides have been investigated.[15,16] Electrode materials play a critical role in identifying the electrochemical behavior of supercapacitors. They are divided into three types: transition metal oxides, conducting polymers, and carbon-based materials, such as graphene, carbon nanotubes, and activated carbon.[17–19] Among these, metal oxides (especially bi- and trimetallic oxides) have been extensively explored in the fields of sensing, medicine, energy, water purification and catalysis.[20–24] Nanostructured transition metal oxides have garnered significant attention because of their ability to store charge through Faradaic reactions, providing superior specific capacitance to electrochemical double-layer materials.[25] Bi_2WO_6 is a representative of Aurivillius phase—layered bismuth tungstates, which features a high potential for redox chemistry and crystalline stability because of alternating layers composed of $(WO_4)^{2-}$ and $(Bi_2O_2)^{2+}$ frameworks. This has been attributed to the fact that these substances have highly favorable electronic configurations with an ability to achieve multiple oxidation levels as well as high faradaic activity.[26]

In recent years, bismuth tungstates, particularly Bi_2WO_6, have received increasing attention for their potential use in electrochemical energy storage. In Bi_2WO_6, the Aurivillius phase with a layered structure provides plenty of redox sites for reactions and promotes the diffusion of ions. Moreover, the presence of Bi^{3+} ions improves the electrochemical reversibility.[27] Compared with traditional monometallic oxides, such as Bi_2O_3 and WO_3, Bi_2WO_6 exhibits higher electrochemical activity due to the synergistic contribution of Bi–O and W–O bonding frameworks, which enable greater redox reactions. Furthermore, during electrochemical cycling, Bi_2WO_6, a layered Aurivillius-type oxide, exhibits both good structural stability and pseudocapacitive activity. Despite these benefits, pure Bi_2WO_6 still has inherent drawbacks that restrict its rate performance and usage in rapid supercapacitors, such as low electrical conductivity and slow ionic transport. To overcome these drawbacks, the integration of Bi_2WO_6 with highly conductive carbon-based materials has been widely reported as such composites effectively enhance charge-transfer kinetics, improve electrolyte accessibility, and mitigate the inherent conductivity limitations of Bi_2WO_6.[28,29] Among different carbon materials, MXenes, which belong to the transition metal carbide and/or nitride category and possess two-dimensional properties, stand out as excellent electrode materials because of their metallic properties, large surface areas, and high resistance to bending.[30] MXenes and their derivatives are increasingly utilized in various applications such as biomedicine, material science and energy storage devices.[31–33]

In addition to ensuring electron transmission channels, the addition of metal oxides to MXenes prevents the agglomeration of metal particles, ensuring the accessibility of the electrolyte. More importantly, the addition of MXene sheets improves ionic conductivity properties by aiding the diffusion of ions at the interface of the electrode and the electrolyte.[34–36] These features make them an excellent choice for forming hybrids with metal oxides for improving charge transport efficiency, facilitating the movement of electrolyte ions, and maintaining the structural integrity of the electrode throughout its cycling.[10,37,38] Besides electrical conductivity, ionic transport properties, such as ionic conductivity, diffusion rate, and cation mobility, are crucial in determining the actual electrochemical properties of SCs. Unfortunately, most of the available literature has focused on compositional and morphological optimization, with less attention given to exploring the underlying relationship between ionic transport properties and electrochemical performance.[39] Among various synthesis methods, hydrothermal synthesis stands out in a league of its own because it provides optimum control over morphology and crystallinity. Moreover, it promotes effective interfacing between different components, which is essential for increasing their synergy in electrochemical studies.[3,40,41]

In this study, we demonstrate the fabrication of a Bi_2WO_6/Bi_2O_3/MXene hybrid electrode that exhibits synergetic improvements in electronic and ionic transport properties. The introduction of MXene not only offers enhanced electrical conductivity but also provides outstanding improvements in the ionic conductivity, ion diffusion, and interfacial charge transfer rate. This remarkable improvement enables the Bi_2WO_6/Bi_2O_3/MXene hybrid electrode to exhibit considerably increased specific capacitance, improved rate capability, and a long cycle life compared to the pristine Bi_2WO_6 electrode. The significance of this study lies in the correlation between the parameters of ionic transport, like ionic conductivity, transference number, or diffusion resistance, and electrochemical properties, allowing a better understanding of ion–electron couplings. This research provides a newly designed Bi_2WO_6/Bi_2O_3/MXene heterostructure for high-performance electrodes for supercapacitors.

2 Experimental

2.1 Chemicals

Bismuth nitrate pentahydrate ($Bi(NO_3)_2 \cdot 5H_2O$), sodium tungstate dihydrate ($Na_2WO_4 \cdot 2H_2O$), MXene ($Ti_3C_2T_x$) and KOH of analytical grade were bought from Sigma-Aldrich and employed in this study.

2.2 Synthesis of Bi_2WO_6/Bi_2O_3/MXene

Bi_2WO_6/Bi_2O_3 and Bi_2WO_6/Bi_2O_3/MXene composites were prepared by a simple hydrothermal method (Fig. 1). Initially, 0.5 g of a bismuth salt and 0.2 g of a tungstate salt were separately dissolved in 30 mL of distilled water and stirred for a few minutes until they were fully dissolved. Then, the two solutions were mixed under intense stirring, and several drops of KOH were

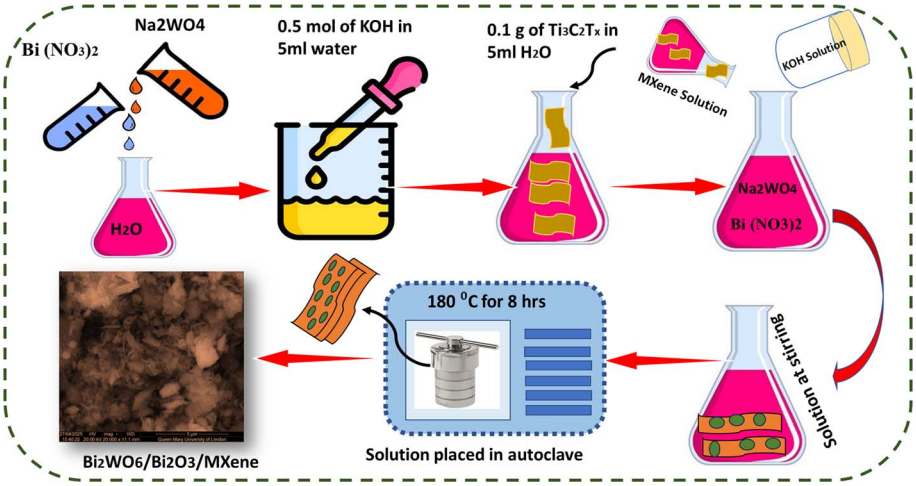

Fig. 1 Schematic of the hydrothermal synthesis of the Bi_2WO_6/Bi_2O_3/MXene composite.

added to adjust the pH value to approximately 7. This mixture was then poured into a Teflon-lined autoclave and heated at 180 °C for 8 hours. After natural cooling to room temperature, the precipitate was collected, washed thoroughly with distilled water and ethanol several times, and dried at 80 °C for 12 hours. Similarly, for the Bi_2WO_6/Bi_2O_3/MXene composite, 100 mg of MXene was added to the bismuth-tungstate solution before the hydrothermal treatment was conducted in the same way as mentioned above.

2.3 Electrochemical testing

The working electrode was prepared by making a slurry of carbon black, a binder and the prepared material in ethanol in the ratio of 1 : 1 : 8. The slurry was uniformly coated onto a nickel foam and dried at 80 °C. This nickel foam was used as the working electrode. Cyclic voltammetry, galvanostatic charge/discharge, electrochemical impedance spectroscopy and cyclic stability measurements were performed in order to study the electrochemical behavior of Bi_2WO_6/Bi_2O_3 and Bi_2WO_6/Bi_2O_3/MXene composites.

3 Results and discussions

3.1 X-ray diffraction (XRD) study

The X-ray diffraction (XRD) patterns of the Bi_2WO_6/Bi_2O_3 and Bi_2WO_6/Bi_2O_3/MXene composites measured at 2θ = 0–80° are shown in Fig. 2a and b, respectively. For both composites, the diffraction peaks at 2θ = 28.59°, 33.11°, 47.39°, 56.10°, 58.41°, and 76.42° can be indexed to the reflections from the (103), (200), (220), (303), (107), and (109) planes of tetragonal Bi_2WO_6 (JCPDS no. 26-1044, space group $I4_1/amd$), respectively, indicating the successful preparation of crystalline Bi_2WO_6 with lattice parameters $a = b = 5.48$ Å and $c = 11.50$ Å. Meanwhile, the detection of the typical peaks at 19.33°, 32.55°, 40.15°, 45.22°, 49.53°, 54.56°, 59.24°, 64.58°, 70.92°, and 72.16°, ascribed to the diffraction planes (−111), (−211), (−222), (023), (−133), (014), (150), (−412), (410) and (025), respectively, can be attributed entirely to monoclinic Bi_2O_3 (JCPDS no. 41-1449), in accordance with the standard pattern, indicating the successful preparation of the dual-phase heterostructure of Bi_2WO_6/Bi_2O_3. From XRD analysis, it is confirmed that Bi_2WO_6 is the dominant primary crystalline phase, while the weak additional peaks assigned to Bi_2O_3 indicate the presence of a minor secondary phase. Bi-rich local surroundings and partial tungstate conversion during hydrothermal synthesis are responsible for the development of Bi_2O_3. For the Bi_2WO_6/Bi_2O_3/MXene composite, the XRD pattern still shows the typical diffraction peaks of both Bi_2WO_6 and Bi_2O_3, establishing the integrity of the crystal structures during the formation of the composites. Results are similar to the previously reported literature.[42] Furthermore, the new diffraction peaks appearing at $2\theta = 9.11°$, 34.45°, and 60.26° can be indexed to the reflections from the (002), (101), and (110) planes of $Ti_3C_2T_x$ MXene (JCPDS no. 52-0857), respectively, confirming its successful integration into the composite matrix. The presence of no extraneous peaks in all samples suggests high phase purity. XRD measurements and X'Pert HighScore Plus's peak intensity ratio approach were used to estimate the compositional ratios of Bi_2WO_6, Bi_2O_3, and MXene in the Bi_2WO_6/Bi_2O_3/MXene composite. According to the findings, Bi_2WO_6 makes up roughly 63.74% of the Bi_2WO_6/Bi_2O_3/MXene composite, Bi_2O_3, 19.11%, and MXene, 17.11%. The average crystallite sizes of the Bi_2WO_6/Bi_2O_3 and Bi_2WO_6/Bi_2O_3/MXene composites, estimated using the Scherrer equation.[43]

$$D = k\lambda/\beta \cos\theta \quad (1)$$

The average size of the crystallite is found to decrease from 49 nm for Bi_2WO_6/Bi_2O_3 to 31 nm upon the addition of MXene, which demonstrates the efficient suppression of crystal growth. The reduction in size greatly promotes the electrochemical properties by improving the number of redox sites accessible and increasing the electrochemically active surface area.

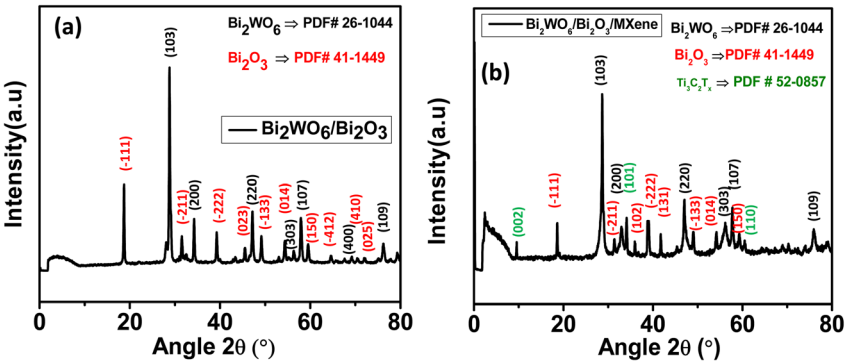

Fig. 2 X-ray diffraction (XRD) spectra of (a) Bi_2WO_6/Bi_2O_3 and (b) Bi_2WO_6/Bi_2O_3/MXene.

3.2 X-ray photoelectron spectroscopy

The exterior surface condition and chemical composition of Bi_2WO_6/MXene were assessed by X-ray photoelectron spectroscopy (XPS). The full-survey spectrum of Bi_2WO_6/MXene obtained from XPS (as shown in Fig. 3a) demonstrates the presence of the constituent elements Bi, W, Ti, C and O in varied oxidation states, with no additional impurity peaks. Fig. 3b depicts the high-resolution spectrum of Bi 4f, in which

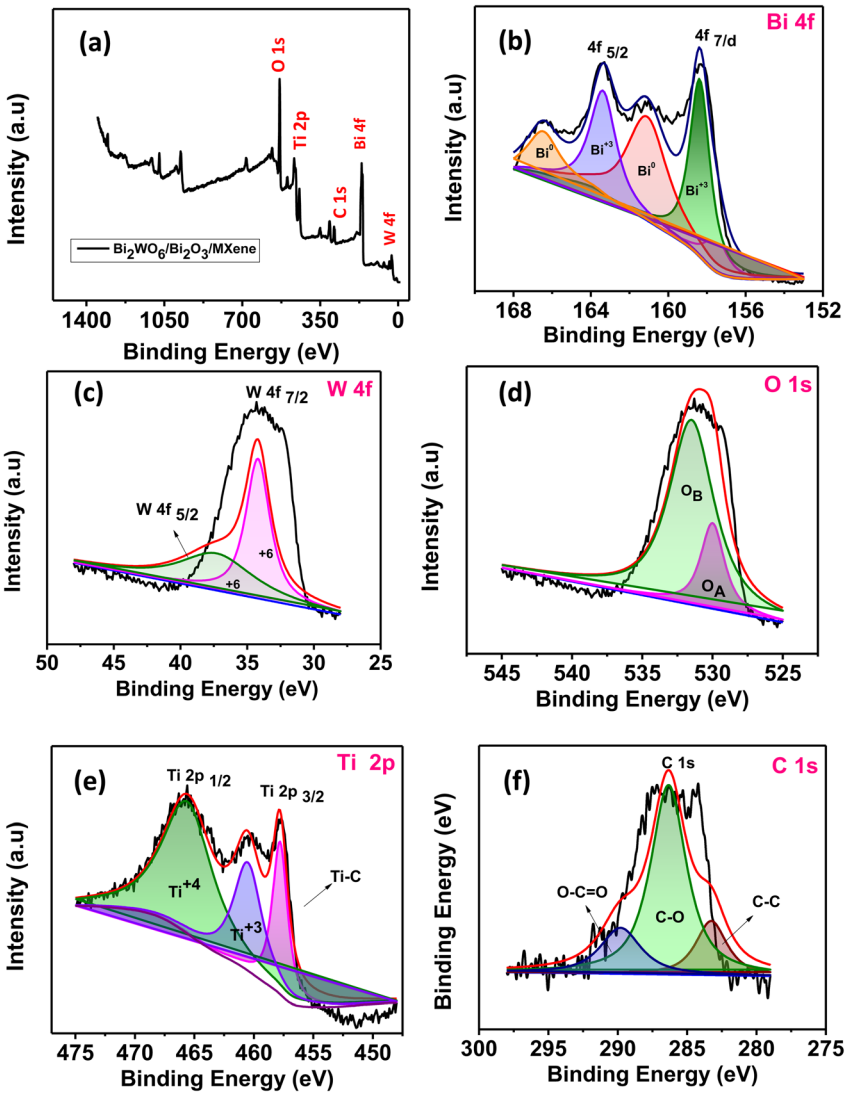

Fig. 3 (a) Survey spectrum of the heterostructured Bi_2WO_6/Bi_2O_3 composite and (b) high-resolution spectra of Bi 4f, (c) W 4f, (d) O 1s, (e) Ti 2p and (f) C 1s.

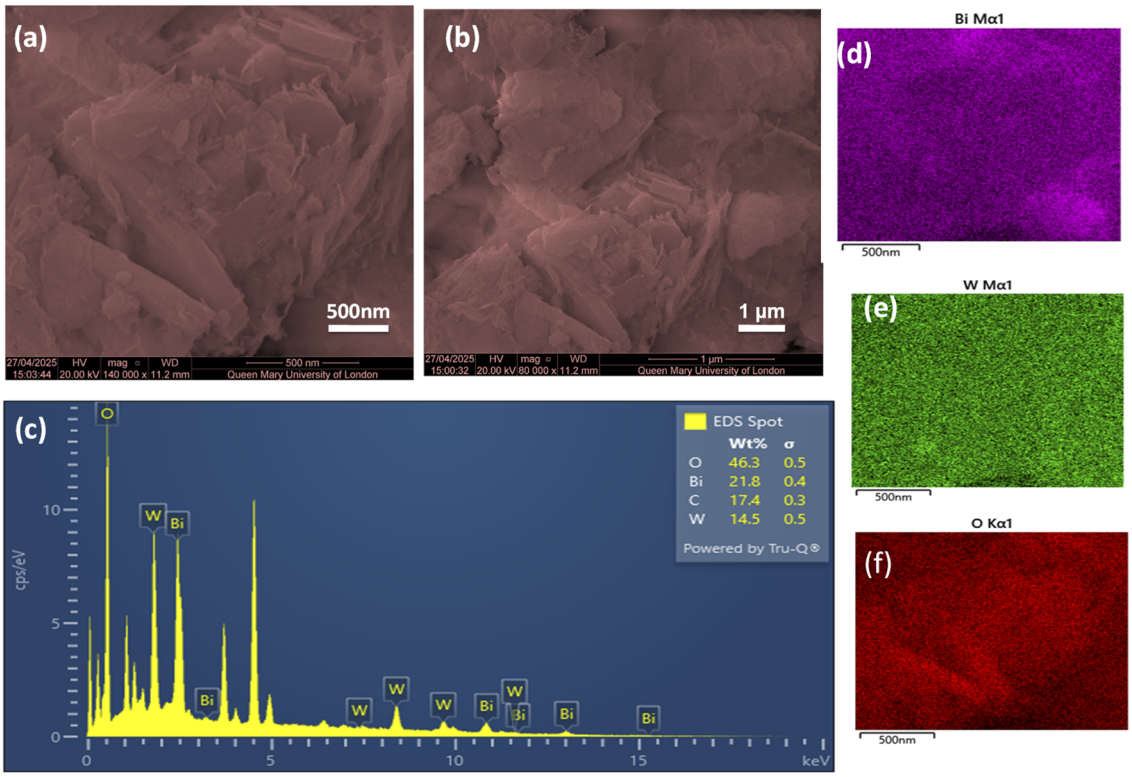

Fig. 4 (a and b) SEM images of Bi_2WO_6/Bi_2O_3 at magnifications of 500 nm and 1 µm, (c) EDX spectrum of the local region of the Bi_2WO_6/Bi_2O_3 composite, and (d–f) EDX mappings of Bi_2WO_6/Bi_2O_3.

the two split peaks at 158.34 eV and 163.33 eV are ascribed to Bi $4f_{7/2}$ and Bi $4f_{5/2}$, respectively, confirming the Bi^{3+} oxidation state with a spin–orbit splitting energy of 4.95 eV.[44] Further deconvolution shows peaks at 161.5 and 166.47 eV, which are ascribed to reduced Bi species (Bi^0 or defect-related Bi) associated with oxygen vacancies.[45]

Fig. 3c shows the high-resolution fitted spectrum of W 4f, with a spin–orbit splitting of 2.1 eV for deconvoluted $4f_{7/2}$ and $4f_{5/2}$ peaks at 35.02 and 37.1 eV, respectively. The fitting validates the presence of the W^{6+} oxidation state in the composite, which is consistent with the expected behavior of Bi_2WO_6. The presence of reduced W states indicates the formation of oxygen vacancies and defect-rich WO_6 units in the Bi_2WO_6 composite.[46–48] Fig. 3d illustrates the high-resolution spectrum of O 1s, whose deconvolution shows different peaks, named as O_A and O_B, at 530.1 and 531.56 eV, respectively. O_A corresponds to lattice oxygen in the WO_6 octahedra, while O_B corresponds to the surface oxygen groups (hydroxyl or defects).[49,50]

Fig. 3e shows the high-resolution spectrum of Ti 2p, in which the deconvoluted Ti $2p_{3/2}$ and Ti $2p_{1/2}$ peaks at 457.3 eV and 460.7 eV are assigned to the Ti–C bonds of MXene and Ti^{3+}, respectively. By contrast, the peak at 466.3 eV corresponds to Ti^{4+}, which indicates partial surface oxidation of Ti_3C_2 in the composite.[51,52] The high-resolution spectrum of C 1s (Fig. 3f) is deconvoluted into different peaks at 284.1, 286.5 and 288.5 eV, which are assigned to C–C, C–O and O–C=O bonds, respectively.[53] This confirms the presence of $Ti_2C_3T_x$ in the composite with some surface oxidation during synthesis.

3.3 Scanning electron microscopy (SEM)

The surface morphology and elemental composition of Bi_2WO_6/Bi_2O_3 and Bi_2WO_6/Bi_2O_3/MXene composites were further investigated by SEM coupled with EDX (Fig. 4 and 5). The SEM images of Bi_2WO_6/Bi_2O_3 at magnifications of 500 nm and 1 µm in Fig. 4a and b show a densely packed and stacked morphology, which is constituted of irregular aggregated plate-like and block-shaped particles. Such compact aggregation can reduce the effective surface area and limit access to the electrolyte. In contrast, the Bi_2WO_6/Bi_2O_3/MXene composite, as we can see in Fig. 5a and b, illustrates a rather open and heterogeneous structure with oxide particles uniformly distributed on the layered MXene sheets. After the incorporation of MXene, a wrinkled and sheet-like framework effectively suppresses the agglomeration of particles, forming interconnected pathways. The particle sizes of the two samples, measured by ImageJ software, are calculated to be 78 nm and 56 nm, respectively, as shown in the histogram in Fig. S1. Noticeable reduction in size of particles make it favorable for enhancement in electrolyte accessibility and ion intercalation or deintercalation, electron transport, and thus enhance the electrochemical performance of the composite electrode. The EDX spectrum (Fig. 4c) of the Bi_2WO_6/Bi_2O_3 sample further confirms that this nanocomposite contains Bi, W, and O elements, verifying the successful formation of the bismuth tungstate oxide phases without detectable impurities, while the elemental EDX mapping (Fig. 4d–g) shows the homogenous distribution of Bi, W, and O.

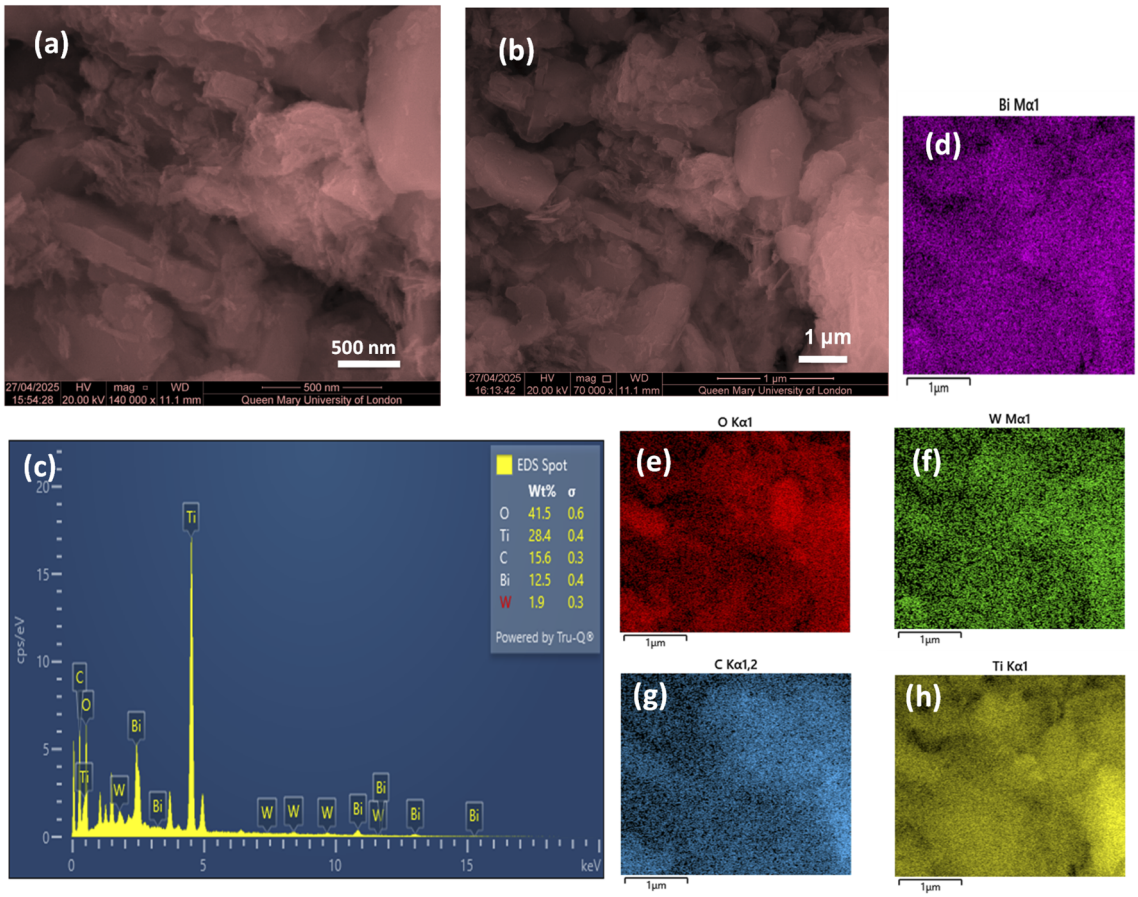

Fig. 5 (a and b) SEM images of Bi_2WO_6/Bi_2O_3/MXene at magnifications of 500 nm and 1 μm, (c) EDX spectrum of the local region of the Bi_2WO_6/Bi_2O_3/MXene composite, and (d–h) EDX mappings of Bi_2WO_6/Bi_2O_3/MXene.

After the addition of MXene, the EDX spectrum of the Bi_2WO_6/Bi_2O_3/MXene composite (Fig. 5c) displays extra Ti and C signals, but all Bi, W, and O signals confirm the successful incorporation of the $Ti_3C_2T_x$ MXene within the composite matrix. Because EDS delivers single local point analysis, the composition may deviate from the bulk-average phase fractions derived by XRD.

Additionally, the elemental EDX mapping images shown in Fig. 5d–h illustrate the homogeneous spatial distribution of Bi, W, O, Ti, and C throughout the composite, suggesting interfacial contact between oxide phases and MXene sheets. These characteristics, namely uniform elemental dispersion and the well-connected morphology, are expected to facilitate effective charge transport and electrolyte accessibility, thereby promoting high electrochemical activity.

3.4 Brunauer–Emmett–Teller (BET) analysis

For BET analysis, nitrogen adsorption–desorption isotherms were measured at 77 K to examine the surface and pore properties of Bi_2WO_6/Bi_2O_3 and Bi_2WO_6/Bi_2O_3/MXene composites. As seen in Fig. 6a, both samples display a characteristic type-IV

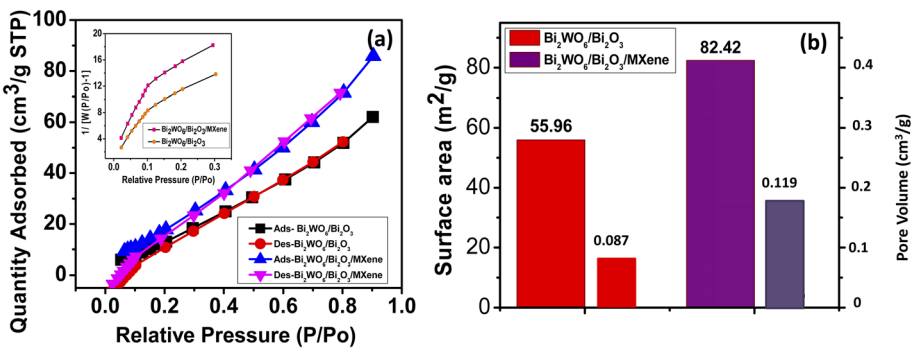

Fig. 6 (a) BET surface area isotherms (N_2 adsorption and desorption) of the Bi_2WO_6/Bi_2O_3 and Bi_2WO_6/Bi_2O_3/MXene composites and (b) comparison of the surface area and pore volume of Bi_2WO_6/Bi_2O_3 and Bi_2WO_6/Bi_2O_3/MXene composites.

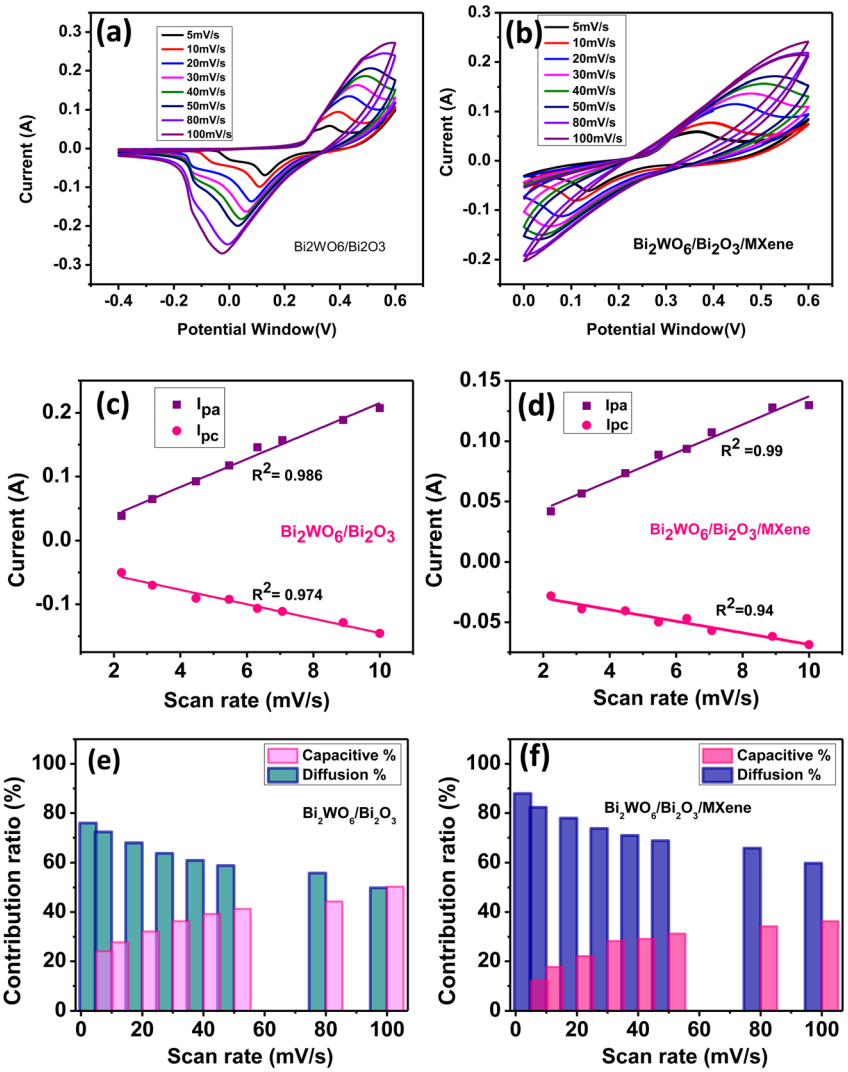

Fig. 7 (a and b) CV curves of Bi_2WO_6/Bi_2O_3 and Bi_2WO_6/Bi_2O_3/MXene at multiple scan rates (5–100 mV s^{-1}), (c and d) calibration of CV curves of Bi_2WO_6/Bi_2O_3 and Bi_2WO_6/Bi_2O_3/MXene, and (e and f) capacitive and diffusion-controlled contributions for Bi_2WO_6/Bi_2O_3 and Bi_2WO_6/Bi_2O_3/MXene at multiple scan rates.

isotherm with a pronounced hysteresis loop in the intermediate relative pressure (P/P_0) region, indicating the mesoporous nature of the samples, as per the IUPAC classification. The adsorption in the low P/P_0 region corresponds to monolayer formation, while the steep rise in the adsorption amount at higher P/P_0 values is attributed to capillary condensation in mesopores. The multipoint BET plot, derived from the linear part of P/P_0 *vs.* $1/W(P/P_0 - 1)$ (inset in Fig. 6a), clearly shows a linear fit, confirming the validity of the BET model in the chosen pressure region. The multipoint BET method based on the adsorption isotherm was employed to determine the specific surface area, while the BJH model based on the desorption isotherm curve was used to determine the pore size and volume distribution. It is worth noting that the Bi_2WO_6/Bi_2O_3/MXene composite has a much larger specific surface area than the pristine Bi_2WO_6/Bi_2O_3 (Fig. 6b), as listed in Table S3. The enhanced surface area of the Bi_2WO_6/Bi_2O_3/MXene composite can be ascribed to the two-dimensional layered structure of MXene, which not only suppresses the agglomeration of Bi_2WO_6/Bi_2O_3 nanoparticles but also provides more accessible adsorption sites. Additionally, the hybridization of MXene with metal oxide components leads to an open mesoporous structure, which favors the penetration of the electrolyte and reduces the diffusion length of ions. These features are highly beneficial for enhanced electrochemical performance as they provide a larger electrochemically active surface area, provide faster ion transport kinetics, and result in more efficient redox site utilization, thus facilitating the fast charge storage and excellent capacitive behavior of the Bi_2WO_6/Bi_2O_3/MXene composite.

3.5 Electrochemical analysis

3.5.1 Cyclic voltammetry (CV). The electrochemical characteristics of the synthesized materials, Bi_2WO_6/Bi_2O_3 and Bi_2WO_6/Bi_2O_3/MXene, were analyzed using a series of tests, including cyclic voltammetry (CV), galvanostatic charge–

discharge (GCD) analysis, and electrochemical impedance spectroscopy (EIS). First, CV analysis was carried out in a three-electrode system with an Ag/AgCl reference electrode, a Pt wire as a counter electrode, and the electrochemically synthesized material as the working electrode with a nickel (Ni) foam substrate in a 2 M KOH electrolyte solution at a scan rate from 5 to 100 mV s^{-1} within the potential window of 0–0.6 V, as shown in Fig. 7a and b. The coexistence of faradaic and capacitive charge-storage processes is demonstrated by the broad redox patterns superimposed on a capacitive background in the CV curves acquired at low scan rates, as shown in Fig. 7a and b. These redox characteristics gradually disappear as the scan rate increases, and the curve of the CV profiles become more quasi-rectangular. This suggests that the current response is increasingly governed by fast surface-controlled capacitive processes, while diffusion-limited faradaic reactions cannot fully respond within the shortened time scale. Additionally, as the scan rate increases, the cathodic peaks move toward lower potentials and the anodic peaks move toward higher potentials (Fig. 7c and d). This is explained by the greater electrochemical polarization brought on by charge-transfer kinetic constraints and neglected internal resistance (iR drop). This type of scan-rate-dependent peak shift and suppression is a well-known feature of pseudocapacitive electrodes and has been extensively reported in the literature.[54–56] The specific capacitances were determined using eqn (2), in which $\int I\mathrm{d}v$ denotes the enclosed area of the CV curve, m is the active mass, ΔV is the potential window, and k is the scan rate.[57]

$$C_s = \frac{\int I \times \mathrm{d}v}{m \times k \times (\Delta V)} \quad (2)$$

The specific capacitances (C_s) of both Bi_2WO_6/Bi_2O_3 and Bi_2WO_6/Bi_2O_3/MXene electrodes decrease from 1202.58 to 267.6 and from 1815.9 to 368.9 F g^{-1}, respectively, as the scan rate increases from 5 to 100 mV s^{-1} (Table S1). The higher capacitances of the Bi_2WO_6/Bi_2O_3/MXene electrode are ascribed to the incorporation of $Ti_2C_3T_x$ MXene, which offers greater charge storage capabilities owing to its increased conductivity and surface redox reactions. Bi_2O_3 and $Ti_3C_2T_x$ MXene mostly contribute through surface-dominated pseudocapacitive processes involving hydroxylated surface sites in the alkaline electrolyte, whereas Bi_2WO_6's charge-storage behavior is often related to the reversible redox activity of Bi- and W-based species (multiple oxidation state), as evidenced by XPS analysis,[58–60] which contribute to the overall electrochemical performance of Bi_2WO_6/Bi_2O_3/MXene, as mentioned below:

$$Bi_2WO_6 + OH^- \leftrightarrow BiOOH + WO_4^{2-} + e^- \quad (3)$$

$$BiOOH + OH^- \leftrightarrow BiO_2^- + H_2O + e^- \quad (4)$$

$$Bi^{3+} + 3OH^- \leftrightarrow Bi(OH)_3 \quad (5)$$

$$Bi(OH)_3 + OH^- \leftrightarrow BiO_2^- + 2H_2O \quad (6)$$

$$W^{6+} + e^- \leftrightarrow W^{5+} \quad (7)$$

$$Ti_3C_2 + 2OH^- \leftrightarrow Ti_3C_2(OH)_2 + 2e^- \quad (8)$$

$$Ti\text{–}O + e^- + OH^- \leftrightarrow Ti\text{–}OH \quad (9)$$

The electrochemical process of the Bi_2WO_6/Bi_2O_3/MXene electrode is dominated by faradaic redox reactions related to Bi, W, and Ti species, which are the primary players in charge storage. Furthermore, $Ti_2C_3T_x$ MXene undergoes surface hydroxylation, which enhances its pseudocapacitive nature, and the 2 M KOH electrolyte provides OH^- ions, which promote ion diffusion and interfacial redox processes. Several analytical methods have been introduced in order to distinguish between the diffusion-controlled and capacitive mechanisms of charge storage. Among these, Dunn's method, reported in 2007, has been widely adopted for kinetic analysis for voltammetric data and is represented[61] using eqn (10). This model was used to identify the contributions of the capacitive and diffusion-controlled processes in the Bi_2WO_6/Bi_2O_3/MXene electrode.

$$I(V) = k_1(V) + k_2(V)^{1/2} = i(\text{capacitive}) + i(\text{diffusion}) \quad (10)$$

In the above expression, $I(V)$ is the current response at potential V and $k_1(V)$ and $k_2(V)$ are the capacitive-controlled and diffusion-controlled parts, respectively. The results obtained indicate the combined effect of the capacitive effect and the diffusion of ions on the net charge-storage capability. Fig. 7e and f depicts the dominance of the diffusion-controlled contribution for Bi_2WO_6/Bi_2O_3 and Bi_2WO_6/Bi_2O_3/MXene electrodes at a scan rate of 20 mV s^{-1}. The values for the diffusion-controlled parts for Bi_2WO_6/Bi_2O_3 are 75.14%, 73.63%, 68.20%, 64.97%, 60.22%, 57.49%, 54.60% and 48.98% and for Bi_2WO_6/Bi_2O_3/MXene are 87.93%, 82.32%, 77.95%, 73.76%, 70.90%, 68.78%, 65.9% and 59.78% at scan rates of 5, 10, 20, 30, 40, 50, 80 and 100 mV s^{-1}, respectively. Higher scan speeds increase the capacitive-controlled contribution by reducing the amount of time available for the diffusion of ions.[62]

3.5.2 Galvanostatic charge/discharge (GCD) analysis. Fig. 8a presents a comparison between the GCD curves recorded for Bi_2WO_6/Bi_2O_3 and Bi_2WO_6/Bi_2O_3/MXene electrodes at a current density of 1 A g^{-1} within the potential window of 0–0.6 V. A nonlinear charge–discharge profile is observed for both electrodes, confirming the dominant faradaic charge-storage mechanism. This is consistent with the results of the CV studies discussed above and indicates that the redox reaction is diffusion-controlled. Among the studied electrodes, the Bi_2WO_6/Bi_2O_3/MXene electrode exhibits the longest discharge time, reflecting enhanced specific capacitance. Accordingly, based on the calculated GCD profile at a current density of 1 A g^{-1} within the potential window of 0–0.5 V using eqn (11), the specific capacities of Bi_2WO_6/Bi_2O_3 and Bi_2WO_6/Bi_2O_3/MXene have been estimated to be 751.28 and 988.69 F g^{-1}, respectively.

$$C_s = I \times t/m \times \Delta V \quad (11)$$

where C_s is the specific capacity (F g^{-1}), I is the discharge current (A), t is the discharge time (s), and m is proportional to the mass of the active material (g).[63] Fig. 8b displays the GCD

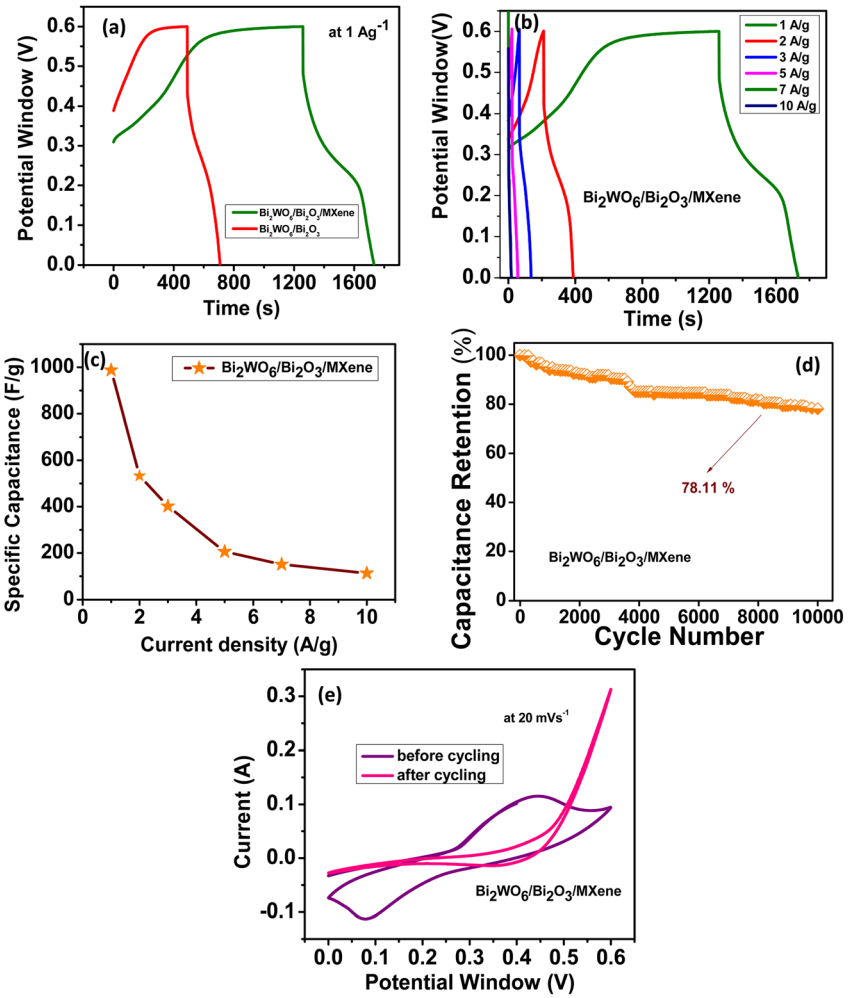

Fig. 8 (a) GCD curves of Bi_2WO_6/Bi_2O_3 and Bi_2WO_6/Bi_2O_3/MXene composites at 1 A g^{-1}, (b) specific capacitance of Bi_2WO_6/Bi_2O_3/MXene at various current densities ranging from 1 to 7 A g^{-1}, (c) specific capacitance of Bi_2WO_6/Bi_2O_3/MXene *vs.* current density, (d) cyclic stability of Bi_2WO_6/Bi_2O_3/MXene, and (e) CV curves of Bi_2WO_6/Bi_2O_3/MXene recorded at 20 mV s^{-1} before cycling and after 10 000 GCD cycles.

curves of the Bi_2WO_6/Bi_2O_3/MXene electrode at different current densities ranging from 1 to 10 A g^{-1}. The specific capacitances of Bi_2WO_6/Bi_2O_3/MXene are found to be 988.69, 533.34, 442.10, 393.38, 274.18, and 108.9 F g^{-1} at current densities of 1, 2, 3, 5, 7, and 10 A g^{-1}, respectively. The high degree of nonlinearity in GCD curves and associated higher voltage values with increasing current density confirm that electrochemically active sites are less accessible in the Bi_2WO_6/Bi_2O_3/MXene nanocomposite, thus resulting in a systematic reduction in its specific capacitance from 988.69 to 108.9 F g^{-1} (Table S2).

The prolonged discharge time and high capacitance of the Bi_2WO_6/Bi_2O_3/MXene electrode can be ascribed to the combined effects of Bi_2WO_6, Bi_2O_3 and $Ti_2C_3T_x$, the improved electrical conductivity, the high diffusion rate of the electrolyte, the high surface area, and the existence of multiple oxidation states for the metallic components, as confirmed by the XPS study. The charge-storage behavior of the composite can be mainly ascribed to Bi_2WO_6, which functions as the primary redox-active framework through reversible Bi–O and W–O surface interactions, as revealed by XRD. Moreover, the minor Bi_2O_3 phase enhances pseudocapacitive charge storage by contributing more Bi-based redox-active sites. In the meantime, the $Ti_3C_2T_x$ MXene offers a highly conductive network that lowers charge-transfer resistance and makes it easier to use the oxide redox sites effectively. Interactions between Bi_2WO_6, Bi_2O_3 and MXene result in better electrochemical performance.[71–73] Fig. 8c exhibits that an increased current density leads to a corresponding decrease in the specific capacitance due to restricted faradaic processes and natural high ohmic drops at a high current density.[74,75] The specific capacitance of the Bi_2WO_6/Bi_2O_3/MXene electrode made using the hydrothermal technique is compared with that of other recently reported materials in Table 1.

Fig. 8d indicates that the Bi_2WO_6/Bi_2O_3/MXene electrode exhibits an excellent capacitance retention of 78.11% of its original capacitance after 10 000 charge/discharge cycles at a current density of 1 A g^{-1}. CV was performed at 20 mV s^{-1} before and after 10 000 GCD cycles in order to determine the cause of the capacitance decline in Fig. 8d. After prolonged cycling, the basic charge-storage mechanism is still intact, as seen by the postcycling CV profile in Fig. 8e. However, slower

Table 1 Comparison of the specific capacitance of recently reported materials with heterostructured Bi_2WO_6/Bi_2O_3/MXene

Sr. no.	Composition	Specific capacitance (C_s)	Current density (A g^{-1})	Synthesis route	Reference
1	Bi_2O_3/FSSM	421.76 F g^{-1}	10 mA cm^{-2}	Hydrothermal	64
2	WO_3/MXene	290 F g^{-1}	0.5 A g^{-1}	—	65
3	Bi_2O_3@rGO	560 F g^{-1}	5 mV s^{-1}	—	66
4	WO_3 nanorods/MXene	297 F g^{-1}	1 A g^{-1}	—	67
5	Bi_2O_3/MXene	613 F g^{-1}	0.6 A g^{-1}	—	68
6	Cu–WO_3/MXene	692 F g^{-1}	1 mA	—	69
7	MWCNT–WO_3	429.6 F g^{-1}	2 mA cm^{-2}	—	70
8	**Bi_2WO_6/Bi_2O_3/MXene**	**988.69 F g^{-1}**	1 A g^{-1}	—	**This work**

charge-transfer/ion-diffusion kinetics and a progressive reduction in electrochemically accessible active sites are suggested by the smaller enclosed CV area and the greater polarization at higher potentials. Long-term cycling-induced microstructural and interfacial changes, including partial pore blockage and active phase agglomeration/restacking, collectively lead to the apparent capacitance decay. This performance feature not only indicates the high specific capacitance but also the superior electrochemical cyclic durability of the Bi_2WO_6/Bi_2O_3/MXene nanocomposite, which makes it highly promising for use as a pseudocapacitor.

3.5.3 Electrochemical impedance spectroscopy (EIS). The charge flow dynamics and interfacial resistances of Bi_2WO_6/Bi_2O_3 and Bi_2WO_6/Bi_2O_3/MXene electrodes were further examined using EIS, and the resulting Nyquist graphs are displayed in Fig. 9a and b. Charge transfer resistance (R_{ct}) at the electrode/electrolyte interface and ion diffusion within the porous electrode (Warburg impedance) together contribute to the Nyquist plots, which typically show a depressed semicircle in the high-to-medium frequency region and an inclined line at low frequencies.[76] It assists in understanding ion movement, the resistance of the interface, and the process of charge transfer over a broad band of frequencies. It gives vital information regarding the resistive and capacitive components of the system simultaneously. In EIS analysis, the real component of the impedance (Z') on the x-axis represents the resistive component, and the imaginary component (Z'') on the y-axis represents the capacitive component.[77–80]

Fig. 9b, depicts a good fit to our experimental data on Bi_2WO_6/Bi_2O_3/MXene, and the tight overlap between the fitted curves and experimental points suggests accurate fitting. The semicircle diameter is relatively large for Bi_2WO_6/Bi_2O_3, suggesting greater R_{ct}, linked to slow ion diffusion and low electronic conductivity. Conversely, the Bi_2WO_6/Bi_2O_3/MXene composite shows smaller semicircles, indicating that the addition of conductive carbon considerably lowers R_{ct} by promoting ion transport *via* the porous carbon network and offering more effective electron transfer routes.

The solution (R_s) and charge transfer resistance (R_{ct}), calculated by ZSimpWin software, for Bi_2WO_6/Bi_2O_3 are 0.62 ohm and 5.34 ohm and for Bi_2WO_6/Bi_2O_3/MXene are 0.27 and 2.23 ohm, respectively. The slight drop in the values of R_s and R_{ct} for Bi_2WO_6/Bi_2O_3/MXene clearly depicts that adding MXene significantly enhances the ion diffusion properties, resulting in better electrical conductivity and rapid charge flow dynamics compared to Bi_2WO_6/Bi_2O_3.

4 Ionic properties

4.1 Ionic conductivity

Ionic conductivity indicates the inherent property of the electrode material to support ion transfer throughout the charge/discharge cycles or faradaic reactions and reduce the resistance for ion diffusion at the electrode/electrolyte interface, thus enhancing charge utilization efficiency and electrochemical reversibility. Ionic conductivity is an important factor that significantly affects the overall performance

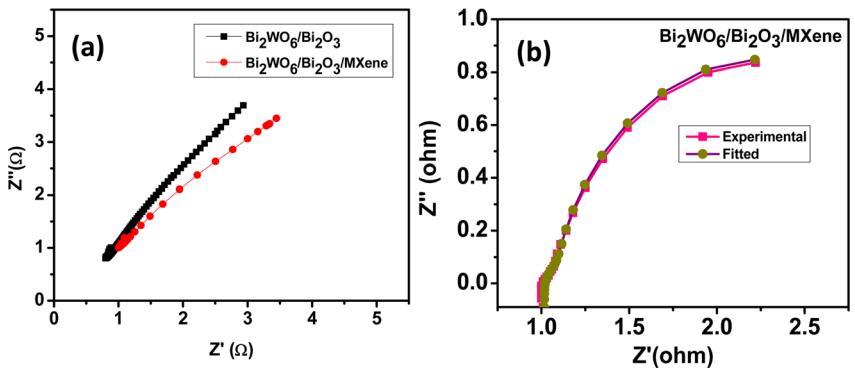

Fig. 9 (a) Nyquist plot of the Bi_2WO_6/Bi_2O_3 and Bi_2WO_6/Bi_2O_3/MXene composites. (b) Nyquist plot of Bi_2WO_6/Bi_2O_3/MXene composite after fitting by ZSimpWin software.

characteristics, particularly of energy storage devices. Faster ionic transport ensures fast electrolyte intrusion into the active material, thus ensuring ready access to electrochemically active sites. Moreover, higher ionic conductivity ensures that polarization resistance and redox reactions occur at a faster rate, hence improving the power performance of the supercapacitor device.[81,82]

$$\sigma = \frac{L}{R_i \times A} \tag{12}$$

The ionic conductivity can be estimated using eqn (12), which gives reliable measurements for the ion transport behavior of the electrode material.[83] In the given equation, R_i represents the ionic resistance corresponding to R_s, as obtained from EIS measurements, while L, A, and σ represent the electrode's thickness, effective cross-sectional area, and ionic conductivity, respectively. From this analysis, the values of ionic conductivity for Bi_2WO_6/Bi_2O_3 and Bi_2WO_6/Bi_2O_3/MXene were estimated to be around 0.097 and 0.085 S cm^{-1}, respectively.

4.2 Transference number

The transference number specifies the portion of the total ion current contributed by cations or anions in an electrolyte solution, and it serves as a foremost indicator of the ion current transport efficacy in supercapacitors or batteries. It depends on multiple factors such as the ion size, ion mobility, association/dissociation reactions, solvent viscosity, temperature, and electrode/electrolyte interface polarization, and its values range from 0 to 1.[81] A larger transference number of cations indicates larger cation transport in the electrolyte solution or larger ion current transport with reduced polarization loss in supercapacitors or batteries. The transference number was calculated using the Sorenson and Jacobsen equation (eqn (13)) and t^+, which represents the cation transference number.

$$t = \frac{1}{1 + W_d/R_b} \tag{13}$$

The anion transference number, t^-, was calculated by the relation $t^- = 1 - t^+$. Here, $W_d(0)$ represents the Warburg constant and R_b represents the electrolyte resistance. According to this theoretical explanation, the values of the cation part for Bi_2WO_6/Bi_2O_3 and Bi_2WO_6/Bi_2O_3/MXene composites have been calculated to be 0.67 and 0.42, respectively, which indicates the higher transport of the ion in the heterostructured nanocomposite.

4.3 Rate constant

The rate constant is a kinetic factor indicating the speed of electrochemical reactions. It gives an estimate of the efficiency of electron transfer from the electrode surface to the ions of the electrolytes in redox reactions, and it is directly linked to R_{ct}. A higher value of the rate constant indicates fast redox reactions, leading to enhanced charge storage capability, improved power performance, and superior electrochemical efficiency of the energy storage device.[55,84]

$$k = RT/(F^2 \times R_{ct} \times C), \tag{14}$$

The rate constant was estimated by eqn (14). In this equation, R and T are the universal gas constant and temperature, respectively, whereas F, R_{ct}, and C are the Faraday constant, charge transfer resistance extracted from electrochemical impedance spectra, and electrolyte concentration, respectively. According to this calculation, the rate constants were estimated to be 3.82×10^{-7} and 3.14×10^{-7} for Bi_2WO_6/Bi_2O_3 and Bi_2WO_6/Bi_2O_3/MXene, respectively.

5 Conclusion

In this work, a novel Bi_2WO_6/Bi_2O_3/MXene composite electrode is fabricated through a hydrothermal approach and investigated for supercapacitor applications. Bi_2WO_6/Bi_2O_3/MXene shows a significant specific capacitance value of 1815.9 at 5 mV s^{-1} (obtained from CV analysis) and 988.69 F g^{-1} (from GCD analysis) with a remarkable cyclic stability of 78.11%. Additionally, Bi_2WO_6/Bi_2O_3/MXene exhibits a significant drop in internal resistance (R_s = 0.27 ohm and R_{ct} = 2.23 ohm). After incorporating MXene, the resultant electrodes exhibit profoundly enhanced electrochemical performances compared to the bare Bi_2WO_6/Bi_2O_3 electrode, as reflected by the improvement in the specific capacitance and charge-transfer kinetics of the thus-prepared Bi_2WO_6/MXene electrode. The superior capacitive performance is ascribed mainly to the strong synergistic effect between Bi_2WO_6 and MXene, where the MXene serves as an excellent conductive scaffold with fast ion diffusion, whereas Bi_2WO_6 offers plenty of redox sites for faradaic capacity accumulation. As such, the synergistic effect promotes the enhanced electroactive surface area and fast ion–electron pairing with weaker polarization during the charge–discharge cycle, thus leading to a higher specific capacitance with greatly improved cycling performance.

In addition, the enhanced dynamic characteristics of ionic transport as well as the decreased internal resistance facilitate efficient electrolyte diffusion and rapid reaction rate processes in the composite electrode. From the above results, it can be seen that the Bi_2WO_6/Bi_2O_3/MXene composite is an effective approach to mitigate the conductivity drawback of metal oxide materials whilst enhancing their charge storage capacity. This work shows the particular promise of the Bi_2WO_6/Bi_2O_3/MXene composite as a novel electrode material for future supercapacitor applications.

Author contributions

Komal Ali Rao: conceptualization, methodology, writing original draft, validation and editing, review, formal analysis, data curation. Javed Ahmad, Muhammad Imran Khan, Muahmmad Ehsan Mazhar: editing and review, data curation. Adel A. El-Zahar, Majed M. Alghamdi and Muhammad Bilal: resources

and review; Waseem Abbas, Iqra Nawaz and Haleema Riaz: methodology and review.

Conflicts of interest

The authors declare that they have no known competing financial interest or personal relationships that could have appeared to influence the work reported in this paper.

Data availability

All data generated or analyzed during this study are included in this article. Furthermore, all related data are available from the authors upon request.

Supplementary information (SI) is available. See DOI: https://doi.org/10.1039/d6ra00310a.

Acknowledgements

The authors extend their appreciation to the Deanship of Research and Graduate Studies at King Khalid University for funding this work through Large Research Groups Project under grant number RGP 2/35/46.

References

1 D. Goyal, *et al.*, Graphene: a path-breaking discovery for energy storage and sustainability, *Materials*, 2022, **15**(18), 6241.
2 A. G. Olabi, *et al.*, Supercapacitors as next generation energy storage devices: properties and applications, *Energy*, 2022, **248**, 123617.
3 F. Ahmad, *et al.*, A highly active, low-cost CoZn ferrite electrocatalyst in oxygen reduction reactions, *Results Chem.*, 2025, **14**, 102095.
4 F. Ahmad, *et al.*, Direct electron transfer chemistry of redox-active enzymes: applications in biosensor development, *Biofuel Bioprod. Biorefining*, 2025, **19**(3), 963–981.
5 M. Khalil, *et al.*, A critical review of biofuel cell cathodes, *Biofuel Bioprod. Biorefining*, 2025, **19**, 2418–2432.
6 S. Lin, *et al.*, Electrochemical insights into the two-step electron transfer mechanism of denitrifying biocathodes, *Energy Environ. Sci.*, 2025, **1**(1), 100004.
7 M. Z. Iqbal, M. M. Faisal and S. R. Ali, Integration of supercapacitors and batteries towards high-performance hybrid energy storage devices, *Int. J. Energy Res.*, 2021, **45**(2), 1449–1479.
8 K. A. Rao, *et al.*, Development of NiCo2O4/rGO nanocomposites for high performance Supercapacitors, *Chem.–Asian J.*, 2025, **20**(15), e00388.
9 G. Sun, *et al.*, Homogeneous and Mechanically Stable SEI Enables Sodium-Metal Batteries for Extreme Working Conditions, *Adv. Funct. Mater.*, 2025, e18451.
10 W. Zhang, *et al.*, Sodiophilic Interface Induces a NaF-Rich Solid Electrolyte Interface for Stable Sodium–Metal Batteries under Harsh Conditions, *Nano Lett.*, 2025, **25**(15), 6092–6100.
11 K. A. Rao, *et al.*, Hydrothermal synthesis of bimetallic spinel MCo2O4/MXene (M= Ni, Zn) composites as efficient supercapacitor electrodes, *Appl. Organomet. Chem.*, 2025, **39**(10), e70390.
12 N. Fatima, *et al.*, Intercalation of carbonate ions into Ce-doped NiCoAl layered double hydroxides using accelerated kinetics for high-performance hybrid supercapacitor electrodes, *New J. Chem.*, 2026, **50**, 1562–1574.
13 S. Li, *et al.*, Fast charging anode materials for lithium-ion batteries: current status and perspectives, *Adv. Funct. Mater.*, 2022, **32**(23), 2200796.
14 A. S. Raikwar and H. S. Panda, A review on nano-structured electrodes for high-performance supercapacitors: panoramic insights across dimensional spectra, *Discov. Electron.*, 2025, **2**(1), 94.
15 S. Mandal, *et al.*, Recent advancement and design in supercapacitor hybrid electrode materials: Bridging the gap between energy and power density, *Chem. Eng. J. Adv.*, 2025, **21**, 100690.
16 Z. Yi-rong, *et al.*, Recent progress on freestanding carbon electrodes for flexible supercapacitors, *N. Carbon Mater.*, 2022, **37**(5), 875–897.
17 M. Minakshi and K. Wickramaarachchi, Electrochemical aspects of supercapacitors in perspective: from electrochemical configurations to electrode materials processing, *Prog. Solid State Chem.*, 2023, **69**, 100390.
18 W. Abbas, *et al.*, Synergistic CuCo2O4/MWCNT nanocomposites: advanced electrode materials for energy storage and catalysis applications, *J. Mater. Sci.: Mater. Eng.*, 2025, **20**(1), 96.
19 X. Yang, *et al.*, Novel design and fabrication of Bi2S3@ NC nanofibers as promising anodes for advanced potassium energy storage, *Electrochim. Acta*, 2025, 148045.
20 J. Y. Lu, *et al.*, Facile microwave-assisted synthesis of Sb2O3-CuO nanocomposites for catalytic degradation of p-nitrophenol, *J. Mol. Liq.*, 2024, **409**, 125503.
21 R. Li, *et al.*, Iridium-induced metal-organic framework honeycomb nanomaterials catalysis: a pathway to boosting hydrogen evolution reaction, *J. Alloys Compd.*, 2025, **1020**, 179345.
22 R. Hu, *et al.*, High-Fidelity Bioelectrodes with Bidirectional Ion–Electron Transduction Capability by Integrating Multiple Charge-Transfer Processes, *Adv. Mater.*, 2024, **36**(35), 2403111.
23 H. Kuang, *et al.*, Dynamic diels-alder reaction crosslinked metal-organic framework/poly (ionic liquid) composite solid electrolyte for lithium-metal batteries, *J. Colloid Interface Sci.*, 2025, 139638.
24 N. D. Radia, *et al.*, Evaluation of the Adsorption Efficiency of Biopolymer Hydrogel Nanocomposite/Nanoclay in Wastewater Dye Removal, *Asian J. Water Environ. Pollut.*, 2024, **21**(4), 47–54.
25 M. Khot and A. Kiani, A review on the advances in electrochemical capacitive charge storage in transition metal oxide electrodes for pseudocapacitors, *Int. J. Energy Res.*, 2022, **46**(15), 21757–21796.

26 A. Gouveia, *et al.*, Electronic structure, morphological aspects, and photocatalytic discoloration of three organic dyes with MgWO4 powders synthesized by the complex polymerization method, *J. Inorg. Organomet. Polym. Mater.*, 2020, **30**(8), 2952–2970.
27 S. Jiang, Y. Zhang and J. Gong, Applications of bismuth-based nanoparticles for the removal of pollutants in wastewater: a review, *Environ. Sci.: Nano*, 2024, **11**(4), 1332–1367.
28 S. Mahmud, N. Zhang and K. N. Kumar, Characterization of bismuth-based photocatalyst for microcystin-LR degradation and mechanism: a critical review, *R. Soc. Open Sci.*, 2025, **12**(5), 241506.
29 I. Boudene, *et al.*, Superior energy storage performance of metastable β-Bi2O3 nanostructured electrode for advanced supercapacitor applications, *J. Energy Storage*, 2025, **136**, 118519.
30 N. Sun, *et al.*, Revealing the intrinsic effects of introduced carbon nanotubes for Bi2O3 energy storage materials, *Electrochim. Acta*, 2022, **409**, 139948.
31 W. Wang, *et al.*, MXene-Based Responsive Hydrogels and Applications in Wound Healing, *ChemistrySelect*, 2024, **9**(32), e202402073.
32 W. Yu, *et al.*, Boosting electromagnetic wave absorbing capacity of Al2O3 coating through in situ generating nano TiO1. 81 from Ti2AlC MAX phases, *Adv. Funct. Mater.*, 2025, **35**(39), 2504393.
33 Z. Hou, *et al.*, Comparative study of the micro-mechanism of functional group selection at TMD-MXene interfaces: WSe2-Ti3C2Tx heterostructures via functional group substitution from group IV, V, VI, and VII as the prototype, *Appl. Surf. Sci.*, 2025, 165599.
34 F. Shahzad, *et al.*, 2D transition metal carbides (MXenes): applications as an electrically conducting material, *Adv. Mater.*, 2020, **32**(51), 2002159.
35 B. Anasori, M. R. Lukatskaya and Y. Gogotsi, 2D metal carbides and nitrides (MXenes) for energy storage, in *MXenes*, Jenny Stanford Publishing, 2023, pp. 677–722.
36 M. S. Javed, *et al.*, Recent progress in the design of advanced MXene/metal oxides-hybrid materials for energy storage devices, *Energy Storage Mater.*, 2022, **53**, 827–872.
37 X. Hui, *et al.*, Interface chemistry on MXene-based materials for enhanced energy storage and conversion performance, *Adv. Funct. Mater.*, 2020, **30**(50), 2005190.
38 Z. Liu, *et al.*, Multivalent Dipole Interactions-Driven Supramolecular Polymer Layer Enables Highly Stable Zn Anode Under Harsh Conditions, *Adv. Energy Mater.*, 2025, 2502010.
39 S. Yi, *et al.*, Recent advances in MXene-based nanocomposites for supercapacitors, *Nanotechnology*, 2023, **34**(43), 432001.
40 V. Tripathi, Hydrothermal method for synthesis of materials, in *Handbook on Synthesis Strategies for Advanced Materials: Volume-I: Techniques and Fundamentals*, Springer, 2021, pp. 131–152.
41 W. Abbas, *et al.*, Study of the electrical properties and electrochemical sensing efficiency of hydrothermally synthesized Sr doped nickel oxide nanomaterials, *Phys. Scr.*, 2022, **97**(7), 075004.
42 N. Motakef-Kazemi, *et al.*, Synthesis and characterization of bismuth oxide nanoparticle by thermal decomposition of bismuth-based MOF and evaluation of its nanocomposite, *Iran. J. Chem. Chem. Eng.*, 2021, **40**(1), 11–19.
43 R. Verma, *et al.*, Effect of calcination temperature on structural and morphological properties of bismuth ferrite nanoparticles, *Ceram. Int.*, 2021, **47**(3), 3680–3691.
44 C. Huang, *et al.*, Synthesis and application of Bi 2 WO 6 for the photocatalytic degradation of two typical fluoroquinolones under visible light irradiation, *RSC Adv.*, 2019, **9**(48), 27768–27779.
45 M. E. Malefane, *et al.*, Triple S-scheme BiOBr@ LaNiO3/CuBi2O4/Bi2WO6 heterojunction with plasmonic Bi-induced stability: deviation from quadruple S-scheme and mechanistic investigation, *Adv. Compos. Hybrid Mater.*, 2024, **7**(5), 181.
46 S. Bera, *et al.*, Effect of metal doping in Bi2WO6 micro-flowers for enhanced photoelectrochemical water splitting, *Ceram. Int.*, 2022, **48**(23), 35814–35824.
47 M. Hojamberdiev, *et al.*, Tuning the morphological structure, light absorption, and photocatalytic activity of Bi2WO6 and Bi2WO6-BiOCl through cerium doping, *Arab. J. Chem.*, 2020, **13**(1), 2844–2857.
48 R. Levinas, *et al.*, Improved photocatalytic water splitting activity of highly porous WO3 photoanodes by electrochemical H+ intercalation, *Front. Chem. Eng.*, 2021, **3**, 760700.
49 Y. Huang, *et al.*, Facile synthesis of Bi/Bi2WO6 nanocomposite with enhanced photocatalytic activity under visible light, *Appl. Catal., B*, 2016, **196**, 89–99.
50 Y. Zhao, *et al.*, Degradation and removal of Ceftriaxone sodium in aquatic environment with Bi2WO6/g-C3N4 photocatalyst, *J. Colloid Interface Sci.*, 2018, **523**, 7–17.
51 S. Lu, *et al.*, Fabrication of TiO2 nanoflowers with bronze (TiO2 (B))/anatase heterophase junctions for efficient photocatalytic hydrogen production, *Int. J. Hydrogen Energy*, 2019, **44**(45), 24398–24406.
52 A. Saeed, *et al.*, Enhancement of photocatalytic CO2 reduction for novel Cd0. 2Zn0. 8S@ Ti3C2 (MXenes) nanocomposites, *J. CO2 Util.*, 2021, **47**, 101501.
53 C. Lai, *et al.*, In situ growth of TiO 2/Ti 3 C 2 MXene Schottky heterojunction as a highly sensitive photoelectrochemical biosensor for DNA detection, *RSC Adv.*, 2023, **13**(24), 16222–16229.
54 Y. Liu, *et al.*, Enhanced supercapacitor performance of Bi2O3 by Mn doping, *J. Alloys Compd.*, 2022, **914**, 165258.
55 A. J. Bard, L. R. Faulkner and H. S. White, *Electrochemical Methods: Fundamentals and Applications*, John Wiley & Sons, 2022.
56 V. Augustyn, P. Simon and B. Dunn, Pseudocapacitive oxide materials for high-rate electrochemical energy storage, *Energy Environ. Sci.*, 2014, **7**(5), 1597–1614.
57 K. A. Rao, *et al.*, Nb 2 CT x MXene integrated DyMn 2 O 5 composites: tailored particle size and enhanced

capacitance for high performance pseudocapacitors, *J. Mater. Chem. C*, 2025, **13**, 13803–13819.
58 M. Qadeer, *et al.*, Bi2WO6 and TiS2 composite nanostructures displaying synergetic boosted energy storage in supercapacitor, *Ceram. Int.*, 2024, **50**(21), 43477–43489.
59 S. Mathew and S. Devi K R, Rationally designed CeO2 decorated Ti3C2 MXene interface for efficient water splitting and enhanced supercapacitor performance, *Colloids Surf., A*, 2024, **684**, 133170.
60 P. Nikhil, *et al.*, Synthesis effect on surface functionalized Ti3C2Tx MXene supported nickel oxide nanocomposites with enhanced specific capacity for supercapacitor application, *J. Energy Storage*, 2023, **72**, 108414.
61 Y. Jiang and J. Liu, Definitions of pseudocapacitive materials: a brief review, *Energy Environ. Mater.*, 2019, **2**(1), 30–37.
62 D. Acharya, *et al.*, In situ transmogrification of nanoarchitectured Fe-MOFs decorated porous carbon nanofibers into efficient positrode for asymmetric supercapacitor application, *J. Energy Storage*, 2023, **63**, 106992.
63 K. A. Rao, M. E. Mazhar and J. Ahmad, Facile hydrothermal synthesis of a tri-metallic Cu–Mn–Ni oxide-based electrochemical pseudo capacitor, *Dalton Trans.*, 2024, **53**(31), 13012–13021.
64 S. A. Mane, *et al.*, Facile synthesis of flower-like Bi2O3 as an efficient electrode for high performance asymmetric supercapacitor, *J. Alloys Compd.*, 2022, **926**, 166722.
65 H. S. Nishad, *et al.*, Temperature driven pseudocapactive performance of WO3/MXene nanocomposite for asymmetric aqueous supercapacitors, *Chem. Eng. J.*, 2024, **495**, 153360.
66 S. M. Mbam, *et al.*, Performance evaluation of Bi2O3@ GO and Bi2O3@ rGO composites electrode for supercapacitor application, *J. Mater. Sci.: Mater. Electron.*, 2023, **34**(18), 1405.
67 C. Peng, *et al.*, WO3 Nanorods/MXene composite as high performance electrode for supercapacitors, *J. Alloys Compd.*, 2019, **810**, 151928.
68 N. M. Shinde and M. Pumera, MXene/Bi2O3 Nanocomposites as Supercapacitors for Portable Electronic Devices, *Energy Fuels*, 2025, **39**(44), 21583–21589.
69 T. J. Jenila, *et al.*, Unraveling the role of MXene (Ti3C2Tx) integrated Cu-doped WO3 nanocomposites via co-precipitation technique for enhanced supercapacitor performance, *Sci. Rep.*, 2025, **15**(1), 25007.
70 P. Anikpa, *et al.*, Asymmetric supercapacitor performance of hydrothermally-synthesized MWCNT-WO3 composite electrode, *J. Energy Storage*, 2024, **81**, 110439.
71 F. Wang, *et al.*, Electrochemical performance of morphologically different Bi2WO6 nanostructures synthesized via a hydrothermal route, *J. Electron. Mater.*, 2017, **46**(1), 182–187.
72 Z. A. Sandhu, *et al.*, Design and synthesis of hybrid Mo-doped Bi_2O_3 nanomaterials as an efficient electrodes for high-performance supercapacitors, *Electrochim. Acta*, 2025, **512**, 145378.
73 M. Naguib, *et al.*, Two-dimensional nanocrystals produced by exfoliation of Ti3AlC2, in *MXenes*, Jenny Stanford Publishing, 2023, pp. 15–29.
74 X. Li, *et al.*, MXene chemistry, electrochemistry and energy storage applications, *Nat. Rev. Chem.*, 2022, **6**(6), 389–404.
75 R. Liu, *et al.*, Constructing heterointerface of Bi/Bi2S3 with built-in electric field realizes superior sodium-ion storage capability, *eScience*, 2023, **3**(4), 100138.
76 M. Y. Perdana, *et al.*, Understanding the behavior of supercapacitor materials via electrochemical impedance spectroscopy: a review, *Chem. Rec.*, 2024, **24**(5), e202400007.
77 N. Anjum, *et al.*, Electrochemical Impedance Analysis of Ti3C2Tx MXene for Pseudocapacitive Charge Storage, *J. Compos. Sci.*, 2025, **9**(3), 139.
78 S. Karmakar, Impedance spectroscopy for electroceramics and electrochemical system, *arXiv*, 2024, preprint, arXiv:2406.15467, DOI: 10.37256/aecm.6120255567.
79 R. Patil and S. Dutta, Intercalation Engineering of 2D Materials at Macroscale for Smart Human–Machine Interface and Double-Layer to Faradaic Charge Storage for Ions Separation, *Adv. Mater. Interfaces*, 2023, **10**(7), 2202137.
80 N. O. Laschuk, E. B. Easton and O. V. Zenkina, Reducing the resistance for the use of electrochemical impedance spectroscopy analysis in materials chemistry, *RSC Adv.*, 2021, **11**(45), 27925–27936.
81 A. Hussain, *et al.*, Synergistically tailored ionic conduction and transport in ZnO/CNTs based electrodes with enhanced electrochemical efficiency in supercapacitors, *Electrochim. Acta*, 2025, 146736.
82 K.-D. Kreuer, Proton conductivity: materials and applications, *Chem. Mater.*, 1996, **8**(3), 610–641.
83 S. Fatima, *et al.*, Microstructural tailoring for enhanced response of carbon nanotube-filled BiMnO3 electrodes, *Mater. Chem. Phys.*, 2025, 131198.
84 S. U. Asif, *et al.*, Ion transport dynamics and cation mobility in hydrothermally synthesized MXene-NiWO 4 composite electrodes for advanced energy storage, *RSC Adv.*, 2025, **15**(50), 43174–43186.